Supplement of Earth Surf. Dynam., 6, 487–503, 2018
https://doi.org/10.5194/esurf-6-487-2018-supplement

Earth Surface Dynamics
Open Access
EGU

Supplement of

The influence of a vegetated bar on channel-bend flow dynamics

Sharon Bywater-Reyes et al.

Correspondence to: Sharon Bywater-Reyes (sharon.bywaterreyes@unco.edu)

Supplement

Channel topography and model grid

LiDAR was flown by Watershed Sciences, Inc. (now Quantum Spatial) for Missoula County on October 30, 2012 with a Leica ALS60 with 3.83 ground points/m^2, providing 1-m resolution topography with a RMSE of 0.03 m. Inundated regions (reflected off water) were manually removed. In-channel bathymetry was measured with RTK-GPS cross-section surveys (Trimble R7 and 5800 with Trimble 5700 base station) augmented by Sonarmite echosounder measurements in non-wadeable areas. Monuments used for the LiDAR survey were occupied with the RTK GPS. Horizontal and vertical agreement of < 0.10 m was found. RTK topographic points were interpolated in the downstream direction, as is appropriate in rivers. RTK point density was 1.25 pts m^{-2}. All topographic points were combined in iRIC, from which we made a curvilinear orthogonal grid with a centerline following the general pattern of the channel over the model domain with an average cell size of 2.5 by 2.5 m for calibration runs, and 5 by 5 m for the remaining runs, with corresponding 841,851 and 210,926 nodes, respectively. We projected Cartesian coordinate flow solution output to the nearest grid cell of a curvilinear grid (2 by 2 m average grid resolution) covering the channel bend of interest (Figure 3), and converted the associated output to streamwise and stream-normal values with a rotation matrix. A piecewise Cubic Hermite Interpolating Polynomial algorithm was applied to reduce artifacts from the transformation.

Model calibration

We surveyed water surface elevation (WSE) with RTK GPS in at least 30 WSE locations per calibration over a 180 m reach length for each calibration flow (see main text). The calibrated runs (Table 1; Fig. S1) had RMSE of 0.11 – to 0.18 m.

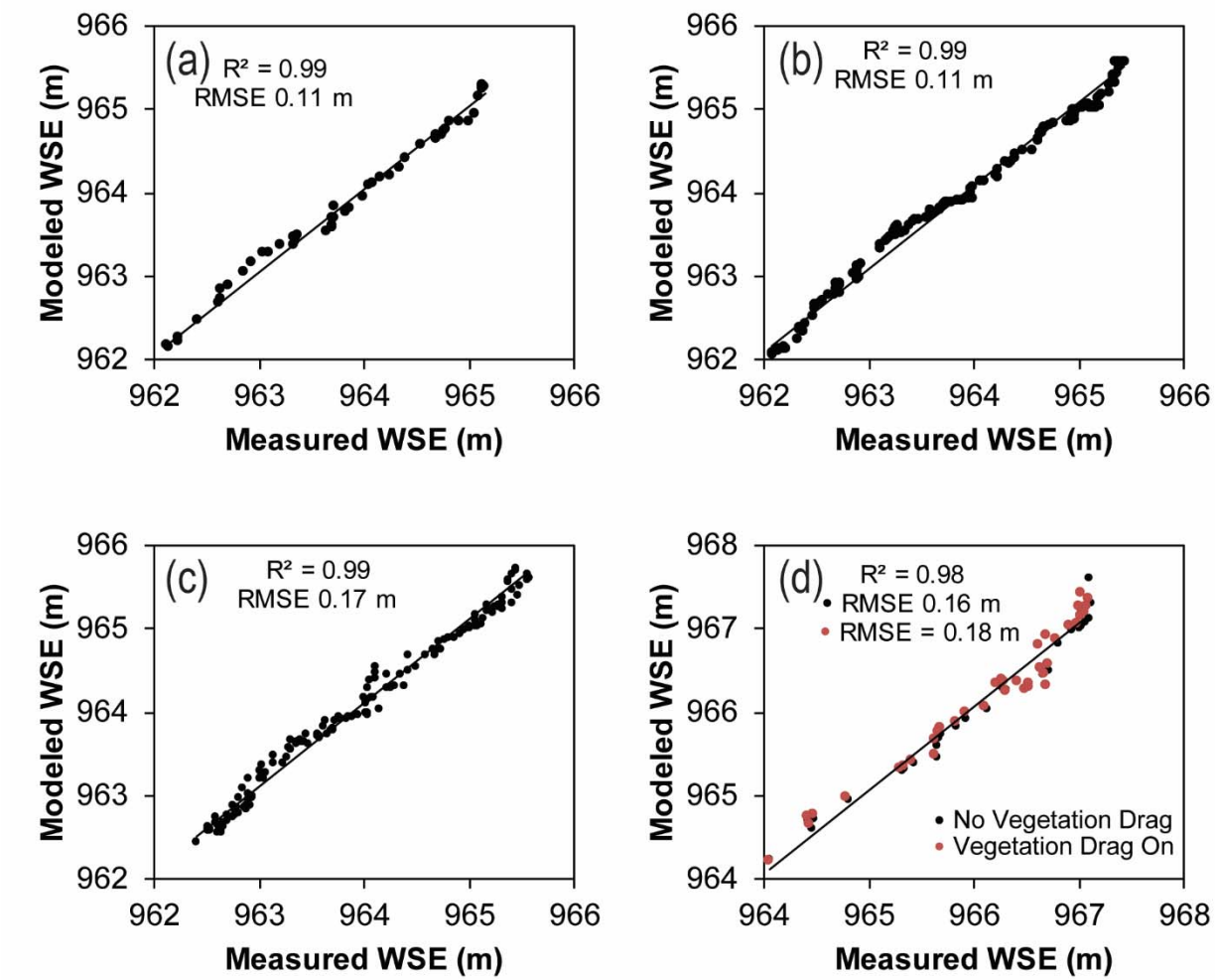

Figure S1. Water surface elevation (WSE) calibration for runs run 1 (a), 2 (b), 3 (c), 4 and 5 (d) (Table 1).

Velocity was measured during base flow in 2015 along cross sections in locations where little geomorphic change was observed following topography collection (Fig. 1) using a Teledyne RD Instruments (TRDI) four beam 1200 kHz Rio Grande ADCP mounted to a 12-ft cataraft equipped with rapid RTK GPS rowed manually. Data were collected using single ping

ensembles with Bottom Mode 12 and Water Mode 7, similar to the methods described in Rennie and Millar (2004), Rennie and Church (2010), and Venditti et al. (2015). Vertical velocity resolution was 0.25 m, with a minimum of four measurements. Velocities from the top 0.5 m and bottom 6 % of the depth were excluded. Velocities were corrected for boat speed with WinRiver II software using bottom tracking. Bed conditions were immobile, so additional corrections were not necessary.

Because velocity profiles were incomplete, data were exported in text format from WinRiver II, and each ensemble post-processed for depth-averaged velocity ($\bar{U}$) in Matlab R2012a by regressing velocity (U) as a function of log of height above the bed (z) to determine shear velocity (u^*) and roughness height (z_o) (Bergeron and Abrahams, 1992). Since U varies as a function of z:

$$U = \frac{u_*}{\kappa} \ln(\frac{z}{z_o}) \qquad \text{(S1)}$$

where κ is the von Karman constant (0.41), the regression of U as a function of z (Uz) yields:

$$U = m_{Uz} \ln(z) + c_{Uz} \qquad \text{(S2)}$$

where m_{Uz} is slope and c_{Uz} the intercept. Shear velocity, $u_{*_{Uz}}$, and roughness height, $z_{o_{Uz}}$, were calculated from the regression coefficients:

$$u_{*_{Uz}} = \kappa m_{Uz} \qquad \text{(S3)}$$

$$z_{o_{Uz}} = \exp(-c_{Uz}/m_{Uz}) \qquad \text{(S4)}$$

Using the law of the wall and our calculated $u_{*_{Uz}}$ and $z_{o_{Uz}}$, we calculated $\bar{U}$ for each ensemble assuming z_m = 0.37H, where H is the total depth:

$$\bar{U} = \frac{u_{*_{Uz}}}{\kappa} \ln(\frac{z_m}{z_{o_{Uz}}}) \qquad \text{(S5)}$$

Individual ensembles are noisy (e.g., Rennie and Church, 2010) and we wished to compare measured $\bar{U}$ to modeled $\bar{U}$. Thus we gridded measured velocities to match model output, ensuring grid cells were concurrent and orthogonal, and calculated the root mean square error (RMSE). We compared the RMSE of law-of-the-wall-derived $\bar{U}$ to a simple average assuming missing values for the top 0.5 m in each ensemble were equal to the value of U corresponding to the largest z. Law-of-the-wall-derived $\bar{U}$ had a lower RMSE, and was thus used instead of the adjusted average (RMSE 0.24 m s^{-1} compared to 0.33 m s^{-1}).

Floodplain vegetation

Individual floodplain trees were mapped (Fig. 1) from the airborne LiDAR, from which vegetation density (#stems m^{-2}), height (m) and diameter (m) were extracted. Vegetation points were isolated and ground vegetation removed with CloudCompare (http://www.danielgm.net/cc/). The dataset was imported as a las dataset in ArcGIS 10.1 and a 1-m resolution raster of maximum height created. Crowns were mapped following a workflow similar to Koch et al. (2006) in ArcGIS 10.1, whereby points were inverted and crowns delineated in a manner similar to delineating drainage basins, and the maximum height for each crown extracted as "basin" minima. Crown "basins" were converted to polygons. Method performance was evaluated by comparing crown polygons to aerial imagery. Nearly every tree large enough to be captured by the LiDAR was accurate (<5 % false positive). Crown attributes (centroid, area, and radius) were calculated using the field calculator. Height of each crown was determined by intersecting centroids with the height raster. Diameter at breast height for each tree was estimated by assuming a crown-diameter to stem-diameter relationship (Hemery et al.,

2005). Although this is a rough estimate, results were reasonable (mean diameter at breast height of 0.20 ± 0.14 m standard deviation).

Vegetation polygons were created by constructing a 15-m bounding polygon. The polygons were smoothed, gaps removed, and dissolved into a single polygon for each region. Average polygon attributes were calculated (vegetation density (#stems m^{-2}), height (m), diameter (m), and A_C (average flow depth multiplied by average diameter at breast height; m^2 per plant).

Supplemental results figures

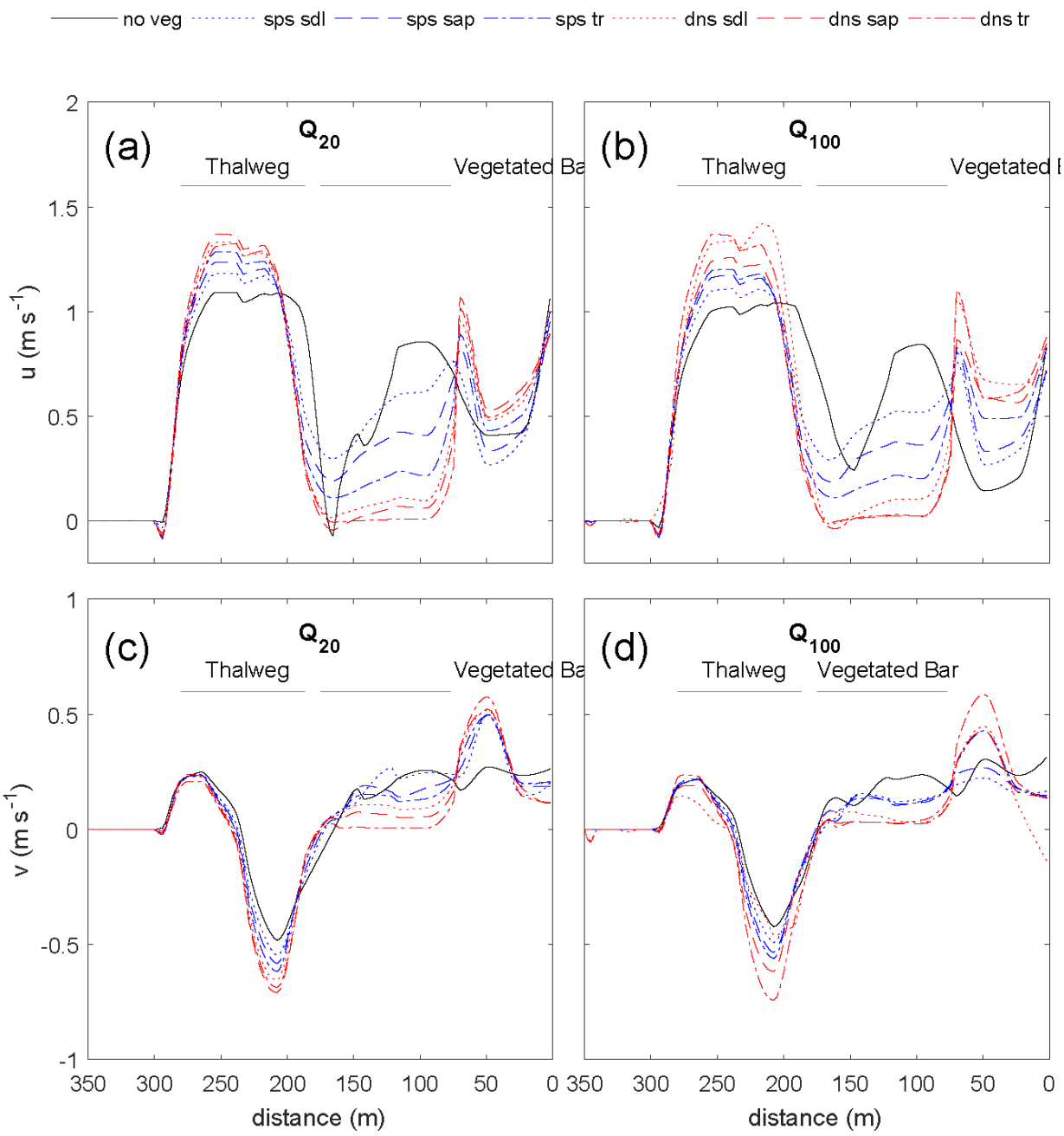

Figure S2. Effect of the vegetated bar (j = 33–75) on the streamwise (u; a,b) and stream-normal (v; c,d) velocity at the downstream cross section (XS1) for the Q_{20} (a,c) and Q_{100} (b,d) flows, with distance from river right end point (Figure 4). With increasing discharge, plant size (seedling to young trees) and density, u is increased and v decreased within the thalweg (j = 100). Both u and v (positive downstream and toward left bank, respectively) are decreased over the bar, and for the sparse young trees and all dense scenarios increased at the edge of the patch. The results for the Q_{20} and Q_{100}, shown here, are similar to the Q_{10} results (Figure 5).

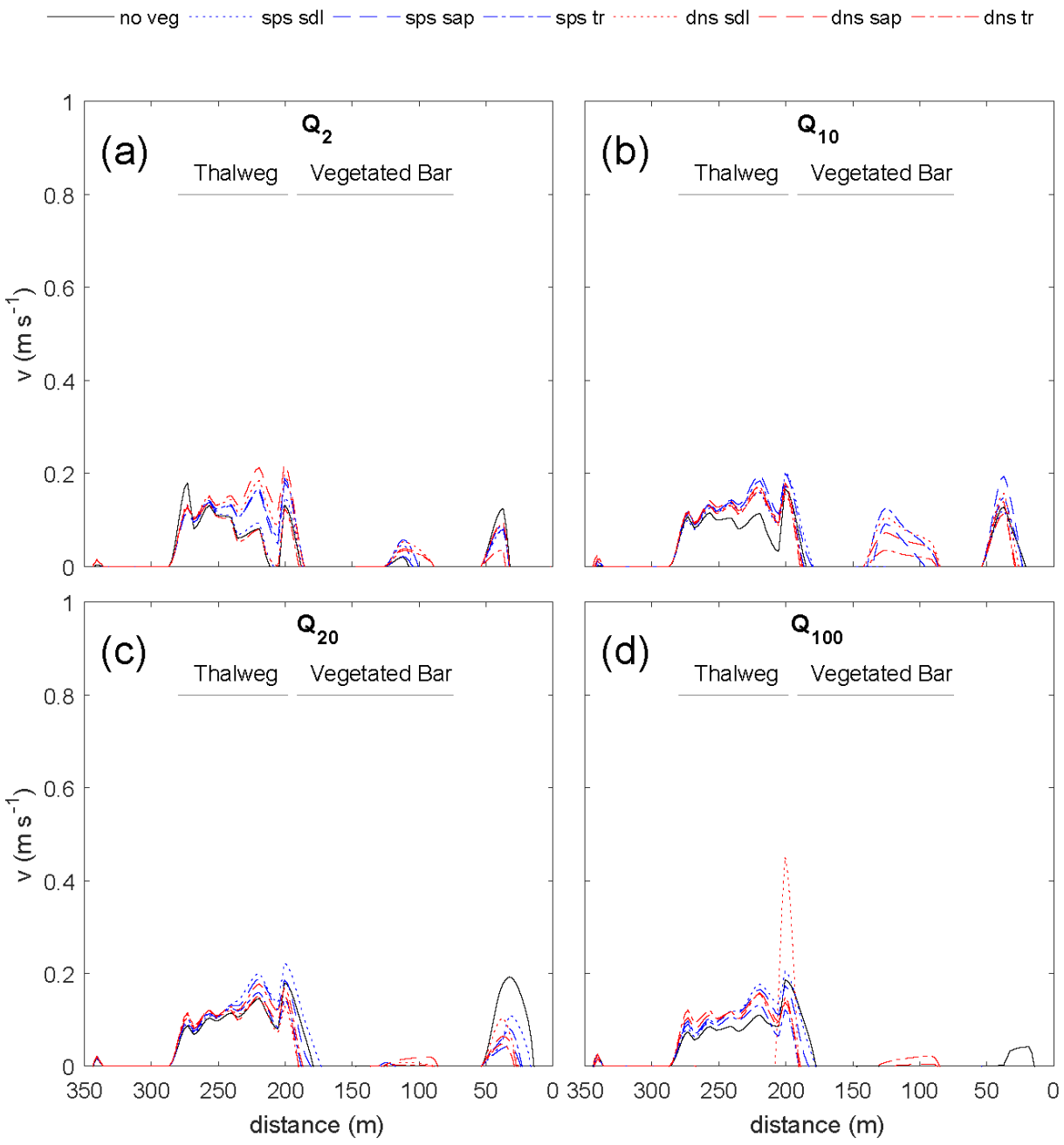

Figure S3. Effect of the vegetated bar (j = 32–82) on the stream-normal (*v*) velocity at the midstream cross section (XS2) for the Q_2 (a), Q_{10} (b), Q_{20} (c), and Q_{100} (d) flows, with distance from river right end point (Figure 4). In general, *v* values are much smaller than *u* values at XS2 (see Figure 6), and not substantially influenced by bar vegetation.

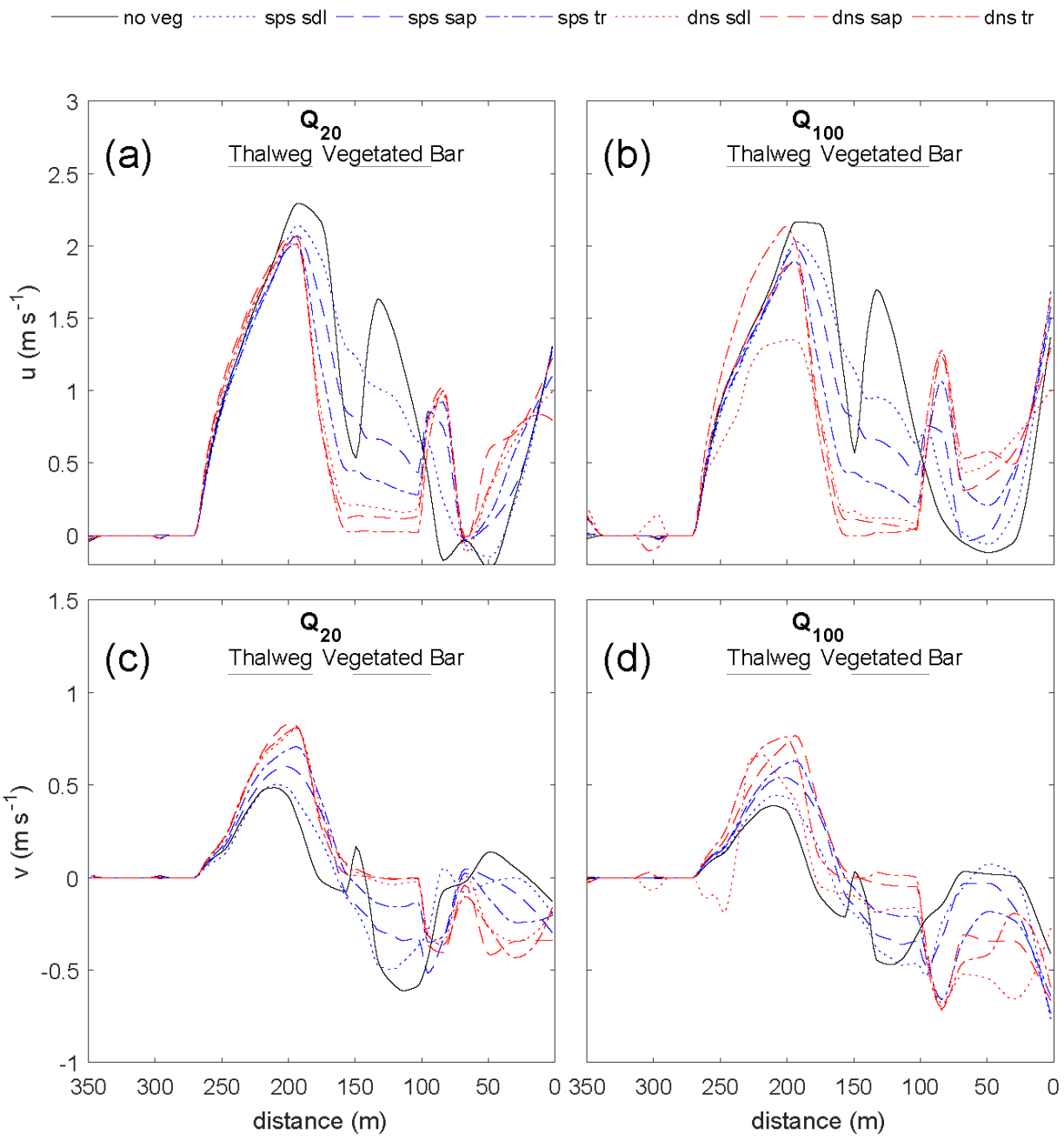

Figure S4. Effect of the vegetated bar (j = 50–65) on the streamwise (*u*; a,b) and stream-normal (*v*; c,d) velocity at the upstream cross section (XS1) for the Q_{20} (a,c) and Q_{100} (b,d) flows, with distance from river right end point (Figure 4). In the thalweg (j = 90) and at the head of the bar, *u* is decreased with increasing seedling size and density. For $Q \geq Q_{10}$, *v* became more negative adjacent to the vegetation patch. The results for the Q_{20} and Q_{100} are similar to that of the Q_{10} flow (shown in Figure 7).

List of terms

A_c = vegetation frontal area (m^2)

c_{Uz} = intercept from regression of U as a function of z

m_{Uz} = slope of regression of U as a function z

u_* = shear velocity

$u_{*_{Uz}}$ = shear velocity calculated from regression U as a function of z

$\bar{U}$ = depth-averaged velocity ($m\ s^{-1}$)

U = velocity ($m\ s^{-1}$)

z_m = height above bed corresponding to law-of-wall-predicted average velocity

z_o = roughness height (m)

$z_{o_{Uz}}$ = roughness height (m) determined from regressing U as a function of z

κ = von Karman constant

References cited

Bergeron, N. and Abrahams, A.: Estimating shear velocity and roughness length from velocit profiles, Water Resour. Res., 28(8), 2155–2158, 1992.

Hemery, G. E., Savill, P. S. and Pryor, S. N.: Applications of the crown diameter–stem diameter relationship for different species of broadleaved trees, For. Ecol. Manage., 215(1–3), 285–294, doi:10.1016/j.foreco.2005.05.016, 2005.

Koch, B., Heyder, U. and Weinacker, H.: Detection of Individual Tree Crowns in Airborne Lidar Data, Photogramm. Eng. Remote Sens., 72(4), 357–363, doi:10.14358/PERS.72.4.357, 2006.

Rennie, C. D. and Church, M.: Mapping spatial distributions and uncertainty of water and sediment flux in a large gravel bed river reach using an acoustic Doppler current profiler, J. Geophys. Res., 115(F3), doi:10.1029/2009JF001556, 2010.

Rennie, C. D. and Millar, R. G.: Measurement of the spatial distribution of fluvial bedload transport velocity in both sand and gravel, Earth Surf. Process. Landforms, 29(10), 1173–1193, doi:10.1002/esp.1074, 2004.

Venditti, J. G., Domarad, N., Church, M. and Rennie, C. D.: The gravel-sand transition: Sediment dynamics in a diffuse extension, J. Geophys. Res. Earth Surf., 120, 1–21,

137 doi:10.1002/2014JF003328.Received, 2015.

138

139